

Hydrogen induced electronic transition within correlated perovskite nickelates with heavy rare-earth composition

Yi Bian^{1†}, Haiyan Li^{1†}, Fengbo Yan^{1†}, Haifan Li¹, Jiaou Wang³, Hao Zhang², Yong Jiang¹, Nuofu

Chen³ and Jikun Chen^{1}*

[†]Y. Bian, H. Li and F. Yan contribute equally to this work.

¹School of Materials Science and Engineering, University of Science and Technology Beijing, Beijing 100083, China

²School of Renewable Energy, North China Electric Power University, Beijing 102206, China

³Beijing Synchrotron Radiation Facility, Institute of High Energy Physics, Chinese Academy of Sciences, Beijing 100049, China

Correspondence: Prof. Jikun Chen (jikunchen@ustb.edu.cn)

Abstract

Although discovery in hydrogen induced electronic transition within perovskite family of rare-earth nickelate ($ReNiO_3$) opens up a new paradigm in exploring both the new materials functionality and device applications, the existing research stays at $ReNiO_3$ with light rare-earth compositions. To further extend the cognition towards heavier rare-earth, herein we demonstrate the hydrogen induced electronic transitions for quasi-single crystalline $ReNiO_3/LaAlO_3$ (001) heterostructures, covering a large variety of the rare-earth composition from Nd to Er. The hydrogen induced elevations in the resistivity of $ReNiO_3$ (R_H/R_0) show an unexpected non-monotonic tendency with the atomic number of the rare-earth composition, e.g., firstly increase from Nd to Dy and afterwards decreases from Dy to Er. Although $ReNiO_3$ with heavy rare-earth composition (e.g. $DyNiO_3$) exhibits large R_H/R_0 up to 10^7 , their hydrogen induced electronic transition is not reversible. Further probing the electronic structures via near edge X-ray absorption fine structure analysis clearly demonstrates the respective transition in electronic structures of $ReNiO_3$ from Ni^{3+} based electron itinerant orbital configurations towards the Ni^{2+} based electron localized state. Balancing the hydrogen induced transition reversibility with the abruptness in the variations of material resistivity, we emphasize that the $ReNiO_3$ with middle rare-earth compositions (e.g. Sm) to be most suitable that caters for the potential applications in correlated electronic devices.

The hydrogen induced electronic phase transitions within d-band correlated metal oxides open up a new paradigm to explore new material functionality and device applications via directly manipulating the orbital occupancy and electronic structures¹⁻³. As a representative such family of material, the rare-earth nickelates ($ReNiO_3$) exhibits exceptional sensitive electronic structures to hydrogen and experiences multiple electronic transitions via chemical/electrochemical hydrogen doping^{1,4,6}. Upon hydrogenations, the typical Mott insulating state of the electron itinerant $t_{2g}^6 e_g^{1\pm 4}$ (or $t_{2g}^6 e_g^1$) orbital configuration based on Ni^{3+} transits towards the highly electron localized $Ni^{2+} t_{2g}^6 e_g^2$ state based on Ni^{2+} . As a result, the material resistivity of $ReNiO_3$ is abruptly elevated reversibly by several orders of magnitudes, while meanwhile maintains high proton conducting properties. The discovery of such hydrogen triggered electronic transition properties beyond conventional semiconductors recently enables new applications, such as ocean electric field sensing⁶, bio-sensing⁷, proton-gated electronic devices^{1,8,9}, neuro-synapse artificial intelligence^{4,10}, and correlated fuel cells⁵.

Nevertheless, the present cognition in the hydrogen induced electronic transitions of $ReNiO_3$ stays at the light rare-earth composition (e.g. Nd, Sm and Eu), from the perspective of both fundamental investigation and device applications^{1,4-6,11}. It is worth noticing that the distinguished advantage for $ReNiO_3$ is the high tolerance in designing its electronic structures and properties via the rare-earth composition occupying the A-site of the distorted perovskite structure (ABO_3)¹². For example, reducing the ionic radius of the rare-earth element (r_{Re}) or enlarging the atomic number of the rare-earth elements causes a more distorted NiO_6 octahedron in crystal structure, and this widens the energy band gap as split from the charge disproportionated Ni^{3+} valance¹²⁻¹⁵. As a result, the relative stability in the insulating or metallic electronic phases can be flexibly regulated via the rare-earth composition, and the respective metal to insulator transition temperature (T_{MIT}) is widely adjustable within a broad temperature range of 100-600 K^{12,16-18}. Analogous to the temperature induced electronic transition, the adjustability in the hydrogen triggered electronic transition properties of $ReNiO_3$ is expected to be largely expanded via further extending the investigations towards heavier rare-earth composition beyond Eu.

In this work, we demonstrate the fundamental relationship between the rare-earth composition and the hydrogen induced electronic transition properties for quasi-single crystalline $ReNiO_3/LaAlO_3$ (001) heterostructures, covering a large variety of the rare-earth composition from Nd to Er. Assisted by the near edge X-ray absorption fine structure (NEXAFS) analysis, the transition in electronic structures and orbital configurations of $ReNiO_3$ upon hydrogenation are demonstrated. A non-monotonic tendency in the hydrogenation elevated material resistivity versus the r_{Re} or the atomic number of the rare-earth composition is discovered, owing to two different competing mechanisms. Balancing the hydrogen induced transition reversibility with

the abrupt change in the variations of material resistivity, we emphasize that the $ReNiO_3$ with middle rare-earth compositions (e.g. Sm) to be most suitable that caters for the potential applications in correlated electronic devices.

The spontaneous electronic transition within $ReNiO_3$ induced by hydrogen was demonstrated to be thermodynamically driven by the material metastability at the Ni^{3+} based $t_{2g}^6 e_g^{1+\Delta}$ (or $t_{2g}^6 e_g^1$) orbital configuration^{11,19,20}. As illustrated in Figure 1a, the hydrogenation reconfigures the electronic structure of $ReNiO_3$ towards electron localized state of Ni^{2+} based $t_{2g}^6 e_g^2$, the process of which meanwhile reduces the positive magnitude in ΔG . It is worth noticing that reducing r_{Re} elevates the ΔG of $ReNiO_3$, the hydrogen induced electronic transitions is expected to be intrinsically dominated by the rare-earth composition.

In Figure 1b and 1c, we show the thermodynamic phase stability of $ReNiO_3$ (e.g. $Re=Nd, Sm, Gd$ and Dy) in the pressure to temperature plane ($P-T$) as predicted according to ref²¹. The dash line represents the merit for $\Delta G=0$ for the heterogeneous growth of $ReNiO_3$, as calculated by the following equation:

$$\Delta G = \Delta H_{LNO,1000K} - T\Delta S_{LNO,1000K} + h(r(Re^{3+}) - r(La^{3+})) - (1/4)RT \ln(P) \quad , \quad \text{where}$$

$\Delta H_{LNO,1000K}$ and $\Delta S_{LNO,1000K}$ are the enthalpy and entropy changes of $LaNiO_3$ at 1000 K, h and s are constants taken from ref²¹, $r(Re^{3+})$ and $r(La^{3+})$ are the ion radius of Re^{3+} and La^{3+} , and R is the ideal gas constant. Nevertheless, the coherent relationship between $ReNiO_3$ and the $LaAlO_3$ (001) substrate is expected to stabilize the metastable phase via interfacial chemical bonds (e.g. -0.23 eV/\AA^2)²², and the respective solid line downwards demonstrate the merit for $\Delta G=0$ by considering such heterogeneous interfacial effect. It can be seen that $ReNiO_3$ with heavier rare-earth composition requires higher magnitude of oxygen partial pressure to stabilize the distorted perovskite structure. As more clearly demonstrated in Figure 1d, at a representative hydrogenation temperature as previously reported (e.g. 100 °C), the $\Delta G=0$ is more positive for $DyNiO_3$ and $GdNiO_3$, compared to $SmNiO_3$ and $NdNiO_3$. Therefore, from a thermodynamic perspective, this shed a light on further improving the hydrogen induced electronic transition properties for using $ReNiO_3$ with heavier rare-earth composition.

To explore how the rare-earth composition impacts the hydrogen induced electronic transition properties of $ReNiO_3$, we grew a serial of $ReNiO_3/LaAlO_3$ samples with various Re compositions, including Nd, Sm, Gd, Dy, Y and Er according to our previous reports²³. The resistances (R) of as-grown films were measured as a function of temperature (T), and their respective $\ln R-1000/T$ tendencies are compared in Figure 2a. The temperature dependence in electronic transportations varies abruptly for $NdNiO_3$, $SmNiO_3$ and $GdNiO_3$ thin film samples, when elevating (or descending) temperature across the T_{MIT} . In contrast, the T_{MIT} for $DyNiO_3$, $YNiO_3$ and $ErNiO_3$

were not measurable, since the metastable thin film samples decomposed when elevating the temperature of characterizations above, e.g. 260 °C, in the Ar atmosphere before reaching their transition temperatures. Nevertheless, the formations of their metastable perovskite phase are demonstrated by the thermistor transportation behavior with large magnitude of negative temperature coefficient resistance (NTCR) in their insulating phase.

According to the previous reports, the insulating phase of $ReNiO_3$ follows a hopping principle in their electrical transportation and the respective thermal activation energy (E_a) can be estimated from their respective $\ln R-1000/T$ tendencies²⁴. In Figure 2b, the magnitude of E_a is further compared for $ReNiO_3/LaAlO_3$, while more details of the fitting are shown in Figure S8 and S9. It can be seen that reducing the r_{Re} enlarges the magnitude of E_a , in particular, near room temperature. This result is in agreement to the increasing tendency in the band gap of $ReNiO_3$ with heavier rare-earth composition^{12,25}, and thereby the carrier (electron) hopping requires to overcome larger energy barrier.

To trigger the electronic transition via hydrogen, dot-shaped platinum pattern was grown on the surface of the $ReNiO_3/LaAlO_3$ (see structure illustration in Figure S10), and afterwards annealed in 20% H_2/Ar mixing gas at 100 °C for 30 minutes. In Figure 3a, the resistances of $Pt/ReNiO_3/LaAlO_3$ as measured between the two adjacent platinum dots are compared before and after the hydrogenation process. Prior to the hydrogenation process, the initial resistance (R_0) of $ReNiO_3$ shows an increasing tendency with a reducing r_{Re} , and this is in agreement to the elevation in the material resistivity for heavier rare-earth composition. The following hydrogenation process significantly enlarges the resistance (R_H), in particular, for $ReNiO_3$ with rare-earth composition lighter than Dy. In Figure 3b, the relative elevation in resistance upon hydrogenation (R_H/R_0) is further compared. It is worth noticing that the R_H/R_0 firstly shows an increasing tendency with a reducing r_{Re} until Dy. Nevertheless, by further reducing r_{Re} towards the heavier rare-earth composition (e.g. Y, Ho and Er), the R_H/R_0 shows a reducing tendency.

The above non-monotonic R_H/R_0-r_{Re} tendency unveils two competing mechanisms in the regulations of the hydrogen induced electronic transition properties of $ReNiO_3$ via the rare-earth compositions, as illustrated in Figure 3c. As already pointed out previously, reducing the r_{Re} is expected to enlarge the positive magnitude in ΔG of $ReNiO_3$, and this provides larger driving force of the hydrogenation that promotes the resultant electronic transition. As a result, the magnitude in R_H/R_0 is elevated by reducing r_{Re} from Nd towards Dy. Nevertheless, the initial material resistivity of $ReNiO_3$ will be increased by reducing r_{Re} , while the metastable phase of $ReNiO_3$ with heavy rare-earth composition (e.g. Dy, Y or Er) is more difficult to be stabilized. It results in the decomposition of these $ReNiO_3$ with heavy rare-earth composition during the hydrogenation process (e.g. into NiO_x and ReO_x), instead of triggering the formation of the expected electron localized electronic phase related to H- $ReNiO_3$.

This explains the afterwards reducing tendency in R_H/R_0 by further reducing r_{Re} from Dy towards Er.

The above understanding is further confirmed by the reversibility in the hydrogenation induced electronic transition of $ReNiO_3$, e.g., by further performing dehydrogenation process to anneal the hydrogenated samples in air at 300 °C for 60 minutes. As shown in Figure 3d, the resistance for $ReNiO_3$ with lighter rare-earth composition (e.g. Sm) recovers to the pristine magnitude upon dehydrogenation. This is in contrast to $ReNiO_3$ with heavy rare-earth composition (e.g. Gd or Dy), in which situation the resistance partially recovered by performing the same hydrogenation and dehydrogenation process.

To further demonstrate the electronic structures of $ReNiO_3$ with various rare-earth compositions during the hydrogen induced electronic transition, the near edge X-ray absorption fine structure (NEXAFS) analysis was performed. Figure 4 shows the NEXAFS spectra of the Ni- L edges and O- K edges for $NdNiO_3$ (Figure 4a and 4b) and $SmNiO_3$ (Figure 4c and 4d) before and after the hydrogenation process. The NEXAFS spectrum of the Ni- L_3 edge reflects the Ni $2p \rightarrow Ni$ $3d$ transition and splits into peak A and B, while the Ni- L_2 edge is associated to Ni-O hybridization strength²⁶. The O- K edge is split into pre-peak A and peaks B and C, where the pre-peak A is attributed to the Ni^{3+} (d^8L) configuration, while peaks B and C are associated to the Ni^{2+} (d^9L) configuration.

A reduction in the relative intensity of the peak B split from peak A within the Ni- L_3 edges is observed for both $SmNiO_3$ and $NdNiO_3$ upon hydrogenation. This demonstrates the decrease in the proportion of $t_{2g}^6e_g^1$ (Ni^{3+}) orbital configuration compared to the $t_{2g}^6e_g^2$ (Ni^{2+})²⁷, indicating a strengthened electron localized electronic phase compared to the electron itinerant one. Further accordant tendency was observed in their NEXAFS spectra of O- K edges, in which case a reduction in the peak A of the O- K edge is observed upon hydrogenation. This indicates a reduced oxygen-projected density of unoccupied electronic states owing to hydrogen induced electron filling, and is in agreement to the increasing proportion in the Ni^{2+} orbital configuration compared to Ni^{3+} .

In summary, we demonstrate the relationship between the rare-earth composition and the hydrogen induced electronic phase transition properties for quasi-single crystalline $ReNiO_3/LaAlO_3$ (001) heterostructures, covering a large variety of the rare-earth composition from Nd to Er. Upon the same hydrogenation process, the magnitude in R_H/R_0 firstly shows an increasing tendency from 10^3 to 10^7 by reducing the r_{Re} from Nd to Dy, and afterwards reduces to 10^2 for further reducing r_{Re} towards Er. The above unexpected non-monotonic R_H/R_0 - r_{Re} tendency reveals the following two competing mechanisms that dominate the hydrogen induced electronic phase properties of $ReNiO_3$ with heavy rare-earth compositions. On the one hand, the larger positive ΔG when reducing r_{Re} promotes the driving force of the hydrogenation

process from the thermodynamic perspective, and this is expected to enlarge R_H/R_0 . On the other hand, the $ReNiO_3$ with smaller r_{Re} exhibits higher initial resistivity and is easier to be decomposed during the hydrogenation process, both of which reduces the R_H/R_0 . Further probing the electronic structures via near edge X-ray absorption fine structure analysis clearly demonstrates the respective transition in electronic structures of $ReNiO_3$ from Ni^{3+} based electron itinerant orbital configurations towards the Ni^{2+} based electron localized state. Balancing the hydrogen induced transition reversibility with the abruptness in the variations of material resistivity, we emphasize that the $ReNiO_3$ with middle rare-earth compositions (e.g. Sm) to be most suitable that caters for the potential applications in correlated electronic devices.

Supplementary material

Supplementary material is available online. Figure S1-S7: $U-I$ of $ReNiO_3$ and $H-ReNiO_3$; Figure S8 and S9: $\ln\rho-1000/T$; Figure S10: $Pt/ReNiO_3/LaAlO_3$.

Acknowledgments

This work was supported by the National Key Research and Development Program of China (No. 2021YFA0718900), National Natural Science Foundation of China (Grant No. 62074014 and 52073090). In addition, JC also acknowledge the support by Beijing New-star Plan of Science and Technology (No. Z191100001119071).

Competing interests

We declare no competing financial interest.

Additional information: Supplementary Information is available for this manuscript.

Correspondence: Prof. Jikun Chen (jikunchen@ustb.edu.cn).

Figures and captions

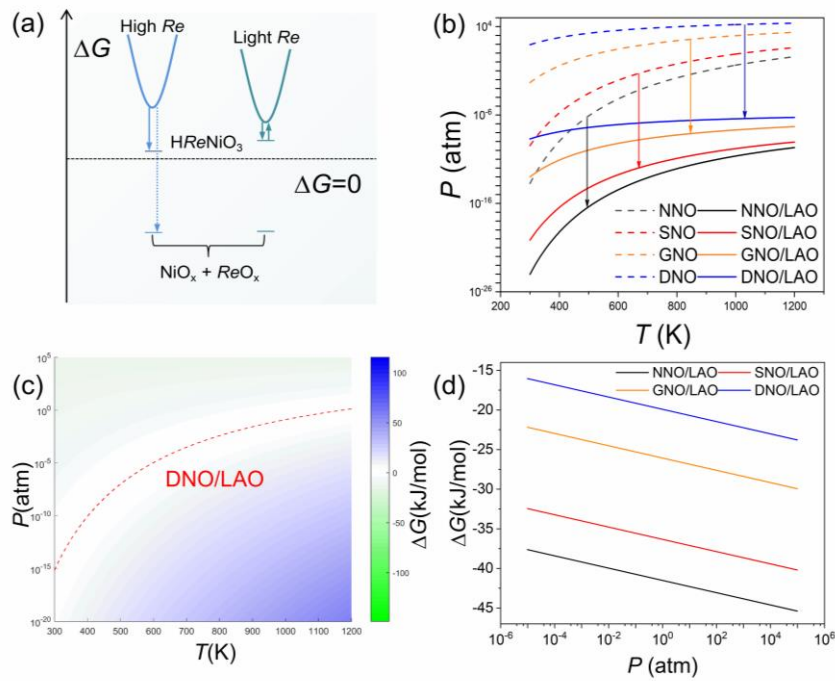


FIG. 1. (a) Illustration of the Gibbs free energy change (ΔG) of $ReNiO_3$ before and after the hydrogenation process. (b) Thermodynamic phase stability diagram for $ReNiO_3$ ($Re=Nd, Sm, Gd$ and Dy) with interfacial reaction. (c) Temperature dependence of the pressure (left: P - T) and the Gibbs free energy change (right: ΔG - T) for $DyNiO_3$ (DNO) on $LaAlO_3$ (LAO). (d) Plot of ΔG vs P for $ReNiO_3/LAO$.

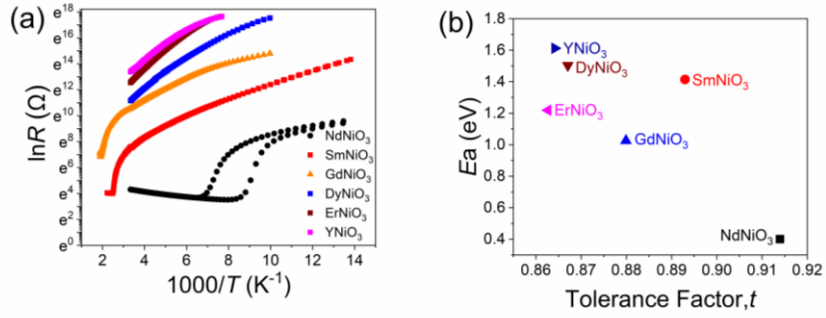


FIG. 2. (a) Temperature dependence of resistivity ($\ln R$) for $ReNiO_3$ ($Re = Nd, Sm, Gd, Dy, Er$ and Y). (b) The thermal activation energy (E_a) of $ReNiO_3$.

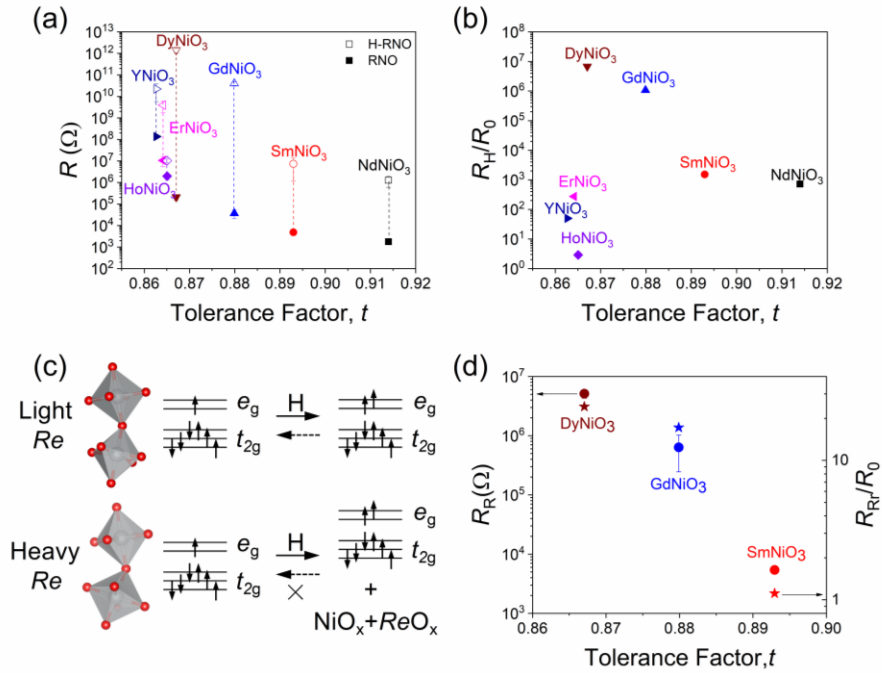


FIG. 3. (a) The resistances of $ReNiO_3$ before and after hydrogenation. (b) The ratio of the hydrogenation resistance and initial resistance (R_H/R_0) of $ReNiO_3$. (c) Illustration of two competing mechanisms in the regulations of the hydrogen induced electronic transition properties of $ReNiO_3$ via the rare-earth compositions. (d) The recovered resistance (R_R) and the ratio of the recovered resistance and initial resistance (R_R/R_0) of $SmNiO_3$, $GdNiO_3$ and $DyNiO_3$.

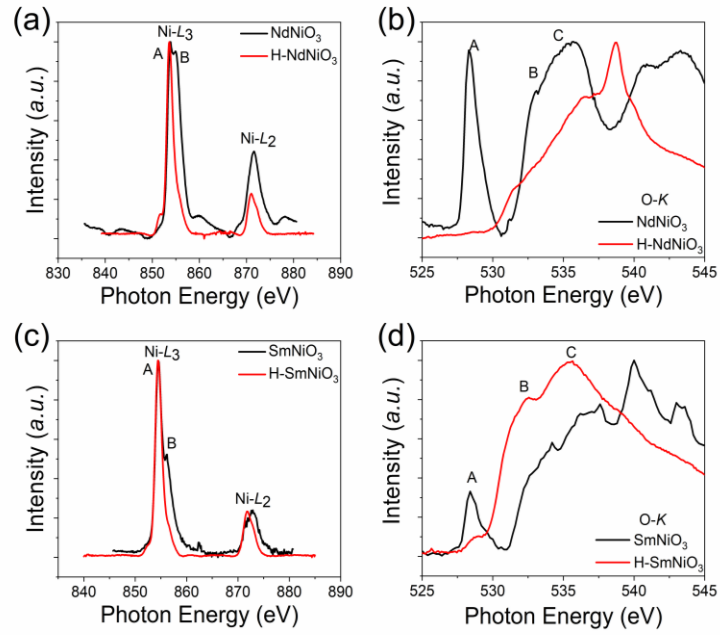


FIG. 4. The NEXAFS spectra of the Ni-L edges and O-K edges for (a) and (b) NdNiO₃, (c) and (d) SmNiO₃.

References

- ¹J. Shi, Y. Zhou, and S. Ramanathan, *Nat. Commun.* **5**, 4860 (2014).
- ²N. Lu, P. Zhang, Q. Zhang, R. Qiao, Q. He, H.-B. Li, Y. Wang, J. Guo, D. Zhang, and Z. Duan, *Nature* **546**, 124 (2017).
- ³H. Yoon, M. Choi, T.-W. Lim, H. Kwon, K. Ihm, J. K. Kim, S.-Y. Choi, and J. Son, *Nat. Mater.* **15**, 1113 (2016).
- ⁴F. Zuo, P. Panda, M. Kotiuga, J. Li, M. Kang, C. Mazzoli, H. Zhou, A. Barbour, S. Wilkins, B. Narayanan, M. Cherukara, Z. Zhang, S. K. R. S. Sankaranarayanan, R. Comin, K. M. Rabe, K. Roy, and S. Ramanathan, *Nat. Commun.* **8**, 240 (2017).
- ⁵Y. Zhou, X. Guan, H. Zhou, K. Ramadoss, S. Adam, H. Liu, S. Lee, J. Shi, M. Tsuchiya, D. D. Fong, and S. Ramanathan, *Nature* **534**, 231 (2016).
- ⁶Z. Zhang, D. Schwanz, B. Narayanan, M. Kotiuga, J. A. Dura, M. Cherukara, H. Zhou, J. W. Freeland, J. Li, R. Sutarto, F. He, C. Wu, J. Zhu, Y. Sun, K. Ramadoss, S. S. Nonnenmann, N. Yu, R. Comin, K. M. Rabe, S. K. R. S. Sankaranarayanan, and S. Ramanathan, *Nature* **553**, 68 (2018).
- ⁷H.-T. Zhang, F. Zuo, F. Li, H. Chan, Q. Wu, Z. Zhang, B. Narayanan, K. Ramadoss, I. Chakraborty, and G. Saha, *Nat. Commun.* **10**, 1 (2019).
- ⁸S. Asanuma, P.-H. Xiang, H. Yamada, H. Sato, I. Inoue, H. Akoh, A. Sawa, K. Ueno, H. Shimotani, and H. Yuan, *Appl. Phys. Lett.* **97**, 142110 (2010).
- ⁹S. D. Ha, U. Vetter, J. Shi, and S. Ramanathan, *Appl. Phys. Lett.* **102**, 183102 (2013).
- ¹⁰H.-T. Zhang, T. J. Park, I. A. Zaluzhnyy, Q. Wang, S. N. Wadekar, S. Manna, R. Andrawis, P. O. Sprau, Y. Sun, and Z. Zhang, *Nat. Commun.* **11**, 1 (2020).
- ¹¹J. Chen, Y. Zhou, S. Middey, J. Jiang, N. Chen, L. Chen, X. Shi, M. Döbeli, J. Shi, J. Chakhalian, and S. Ramanathan, *Appl. Phys. Lett.* **107**, 031905 (2015).

- ¹²G. Catalan, *Phase Trans.* **81**, 729 (2008).
- ¹³J. Alonso, M. Martínez-Lope, M. Casais, J. García-Muñoz, and M. Fernández-Díaz, *Phys. Rev. B* **61**, 1756 (2000).
- ¹⁴P. Canfield, J. Thompson, S. Cheong, and L. Rupp, *Phys. Rev. B* **47**, 12357 (1993).
- ¹⁵F. Conchon, A. Boulle, R. Guinebretière, C. Girardot, S. Pignard, J. Kreisel, F. Weiss, E. Dooryhée, and J.-L. Hodeau, *Appl. Phys. Lett.* **91**, 192110 (2007).
- ¹⁶P. Lacorre, J. B. Torrance, J. Pannetier, A. I. Nazzal, P. W. Wang, and T. C. Huang, *J. Solid. State. Chem.* **91**, 225 (1991).
- ¹⁷I. Vobornik, L. Perfetti, M. Zacchigna, M. Grioni, G. Margaritondo, J. Mesot, M. Medarde, and P. Lacorre, *Phys. Rev. B* **60**, R8426 (1999).
- ¹⁸S. Catalano, M. Gibert, J. Fowlie, J. Iniguez, J.-M. Triscone, and J. Kreisel, *Rep. Prog. Phys.* **81**, 046501 (2018).
- ¹⁹J. Chen, W. Mao, L. Gao, F. Yan, T. Yajima, N. Chen, Z. Chen, H. Dong, B. Ge, P. Zhang, X. Cao, M. Wilde, Y. Jiang, T. Terai, and J. Shi, *Adv Mater* **32**, e1905060 (2020).
- ²⁰J. Chen, W. Mao, B. Ge, J. Wang, X. Ke, V. Wang, Y. Wang, M. Döbeli, W. Geng, and H. Matsuzaki, *Nat. Commun.* **10**, 1 (2019).
- ²¹R. Jaramillo, F. Schoofs, S. D. Ha, and S. Ramanathan, *J. Mater. Chem. C* **1**, 2455 (2013).
- ²²F. Yan, Z. Mi, J. Chen, H. Hu, L. Gao, J. Wang, N. Chen, Y. Jiang, L. Qiao, and J. Chen, (2021), p. arXiv:2111.13308.
- ²³J. Chen, H. Hu, J. Wang, T. Yajima, B. Ge, X. Ke, H. Dong, Y. Jiang, and N. Chen, *Mater. Horiz.* **6**, 788 (2019).
- ²⁴G. Catalan, R. M. Bowman, and J. M. Gregg, *Phys. Rev. B* **62**, 7892 (2000).

- ²⁵M. Escote, A. Da Silva, J. Matos, and R. Jardim, *J. Solid. State. Chem.* **151**, 298 (2000).
- ²⁶Y. Kumar, A. Pratap Singh, S. Sharma, R. Choudhary, P. Thakur, M. Knobel, N. Brookes, and R. Kumar, *Appl. Phys. Lett.* **101**, 112103 (2012).
- ²⁷K. Kleiner, J. Melke, M. Merz, P. Jakes, P. Nagel, S. Schuppler, V. Liebau, and H. Ehrenberg, *ACS Appl. Mater. Interfaces* **7**, 19589 (2015).